Supplementary Information

Bioanalytic resilient nanostructured microneedle longitudinally monitors renal and hepatic drug clearance and dysfunction

Jialun Zhu, *et al.*

Corresponding author: Sam Emaminejad, emaminejad@ucla.edu

This PDF Includes:

- Supplementary Materials and Methods
- Fig S1 to S35
- Table S1 to S2
- Legend for data file S1
- Legend for movie S1

Supplementary Materials and Methods

Materials and reagents

All reagents including the aptamers were purchased from Sigma-Aldrich unless stated. Tris(2-carboxyethyl)phosphine hydrochloride (TCEP) was purchased from TCI America Inc. Tobramycin (900 µg/mg), phosphate-buffered saline (PBS; 1×, pH 7.2; Gibco), PrestoBlue cell viability reagent, calcein-AM, ethidium homodimer-1 (EthD-1), Dulbecco's modified eagle medium, fetal bovine serum, acetone, ethanol, nitric acid (68-70% solution in water) and HPLC water were purchased from Thermo Fisher Scientific. Gold plating solution Elevate Gold 7990 was purchased from Technic Inc. PDMS (Sylgard 184 Silicone Elastomer) was purchased from Dow Corning. Gold-plated acupuncture needles were purchased from Suzhou Acupuncture and Moxibustion Appliance Co. Ltd. The lancets (30 gauge) were from LotFancy Inc. Ag/AgCl ink was purchased from Ercon Incorporated.

Deriving PK parameters from peripheral recordings

The following sections outline the mathematical framework and practical considerations for deriving pharmacokinetics from peripheral recordings.

1. Two-compartment PK model

Two-compartment pharmacokinetic (PK) models represent the body as a central compartment (e.g., blood and rapidly equilibrating organs) and a peripheral compartment (e.g., tissues with slower drug distribution, such as skin). The drug transfer between these compartments and its elimination are governed by the following ordinary differential equations (ODEs):

$$\frac{dX_C}{dt} = k_{21}X_p - k_{12}X_C - k_{10}X_C, \quad \frac{dX_p}{dt} = k_{12}X_C - k_{21}X_p \qquad (S1)$$

where X_C and X_P represent drug concentrations in the central and peripheral compartments, respectively. The constants k_{12}, k_{21}, and k_{10} denote inter-compartmental transfer and elimination rates (Fig. S1).

For a single-dose drug injection administered at t = 0, the ODE solutions are:

$$X_C = \frac{X_0(\alpha - k_{21})}{\alpha - \beta} e^{-\alpha t} + \frac{X_0(k_{21} - \beta)}{\alpha - \beta} e^{-\beta t} \qquad (S2)$$

$$X_P = \frac{k_{12}X_0}{\alpha - \beta}\left(e^{-\beta t} - e^{-\alpha t}\right) \qquad (S3)$$

Here, $X_0 = m_0/V_C$ is the initial blood drug concentration (peak blood concentration), m_0 is the injected drug amount, V_C is the volume of distribution in the central compartment, and α and β are hybrid rate constants:

$$\alpha = \frac{(k_{12} + k_{21} + k_{10}) + \sqrt{(k_{12} + k_{21} + k_{10})^2 - 4k_{21}k_{10}}}{2} \tag{S4}$$

$$\beta = \frac{(k_{12} + k_{21} + k_{10}) - \sqrt{(k_{12} + k_{21} + k_{10})^2 - 4k_{21}k_{10}}}{2} \tag{S5}$$

These solutions can be simplified as:

$$X_{\mathrm{C}} = Ae^{-\alpha t} + Be^{-\beta t},\ X_{\mathrm{P}} = Y\left(e^{-\beta t} - e^{-\alpha t}\right) \tag{S6}$$

where:

$$A = \frac{X_0(\alpha - k_{21})}{\alpha - \beta},\ B = \frac{X_0(k_{21} - \beta)}{\alpha - \beta},\ Y = \frac{k_{12}X_0}{\alpha - \beta} \tag{S7}$$

2. Fitting peripheral PK measurements

Assuming negligible sensor response time compared to PK timescales and linear sensor operation with a calibration factor U, the peripherally recorded signal $R(\mathrm{t})$ is directly related to X_{P}:

$$R(t) = U \cdot X_{\mathrm{P}} = UY \cdot \left(e^{-\beta t} - e^{-\alpha t}\right) = Z \cdot \left(e^{-\beta t} - e^{-\alpha t}\right) \tag{S8}$$

where $Z = \frac{Uk_{12}X_0}{\alpha - \beta}$ (based on Equation S5). Parameters Z, α, and β can be determined via regression fitting of the device recording.

3. Pre-calibration based on inter-compartmental equilibrium diffusion dynamics

To derive pharmacokinetic parameters from peripheral measurements, an effective calibration strategy is essential. However, the sensor calibration factor U, as defined, remains inaccessible with current technology. This limitation arises because ISF is not readily or instantaneously harvestable, and sensor responses vary across tissue types and beaker test due to differences in local electrical impedance.

Our approach combines device-level calibration (based on the factor U) with a biological calibration factor that accounts for blood-to-ISF conversion. The biological calibration is defined by the dimensionless inter-compartment diffusion coefficient $\varepsilon = k_{12}/k_{21}$. ε can be calculated as the ratio of the area-under-the-curve (AUC) of drug concentration in ISF versus blood or as the ratio of ISF and blood drug concentrations when the peripheral concentration peaks (i.e., $t = t_{\max}$, when $\mathrm{d}X_{\mathrm{p}}/\mathrm{d}t = 0$). The latter approach simplifies pre-calibration, practically requiring only one or two blood samples collected and analyzed at or near $t_{\max}$.

Our definition of ε offers two key advantages. First, its ratiometric nature reduces the impact of biological confounders by minimizing the influence of common-mode variables, such as blood flow, vascularization, and membrane permeability, which tend to proportionally affect both k_{12}

and k_{21}. Second, as shown in Section 4, ε always appears alongside U in the expressions for clinically relevant PK parameters, enabling the definition and application of a unified calibration factor, $U^* \equiv \varepsilon \cdot U$, for mapping peripheral parameters to PK parameters. Notably:

$$U^* \equiv \epsilon \cdot U = \frac{R(t_{\mathrm{max}})}{X_{\mathrm{C}}(t_{\mathrm{max}})} \qquad (S9)$$

The unified factor can be pre-characterized (Study 1, Fig. 5), using peripheral tissue recordings and minimal blood sampling, enabling pre-programmed PK analysis during clinical deployment (Study 2, Fig. 5). With this U^* acquired, neither U nor ε need to be known individually for the calculation of PK parameters.

This ratiometric formulation makes ε a reflection of partitioning behavior that is less sensitive to common-mode physiological confounders—such as changes in blood perfusion—which affect both k_{12} and k_{21} proportionally. Under the steady-state conditions of a two-compartment pharmacokinetic model (Fig. S3), the intercompartmental clearance Q is given by

$$Q = k_{12}V_{\mathrm{C}} = k_{21}V_{\mathrm{P}} \qquad (S10)$$

where V_{C} and V_{P} are the fixed volumes of the central and peripheral compartments, respectively. Perfusion-driven changes in Q therefore alter k_{12} and k_{21} proportionally, but their ratio, $\varepsilon = k_{12}/k_{21}$, remains theoretically constant and is empirically less affected.

For example, in a study of postpartum pharmacokinetics (*91*), Q decreased nearly ten-fold over 15 weeks, yet ε changed by only about two-fold, supporting the robustness of this ratiometric strategy under significant physiological variation. Although ε is relatively stable within a given tissue type, its value can vary across tissues owing to differences in matrix composition, permeability, and impedance. In the present study, all pharmacokinetic data (Fig. 5) were derived from dermal tissue, ensuring consistency in U^* across experimental conditions.

4. Calculation of PK parameters from peripheral measurements

Key PK parameters, including half-life, total drug exposure, and clearance, can be derived from peripheral recordings using the pre-calibration factor U^* and fitted parameters Z, α, and β.

a. Half-life $t_{1/2}$: The half-life represents the time required for the concentration of a drug in the body to decrease by half due to elimination processes. It is a critical parameter in determining dosing regimens, as it reflects the persistence of the drug in systemic circulation. The half-life can be calculated from the exponential decay term of the concentration-time profile:

$$t_{1/2} = \frac{ln(2)}{\beta} \qquad (S11)$$

b. Total drug exposure (area under the curve, *AUC*): The *AUC* quantifies the total exposure to the drug over time and is expressed as the integral of the concentration-time curve:

$$\mathrm{AUC} = \int_0^{\infty} X_{\mathrm{C}}\mathrm{dt} = \frac{Z(\alpha-\beta)}{\epsilon U\alpha\beta} = \frac{Z(\alpha-\beta)}{U^{*}\alpha\beta} \qquad (S12)$$

c. Drug clearance (*CL*): This parameter captures the body's efficiency in eliminating the drug. It is defined as the volume of plasma cleared of the drug per unit time and is calculated as:

$$CL(t) = \frac{\text{Rate of elimination}}{X_{\mathrm{C}}(t)} = \frac{V_C \frac{dX_{\mathrm{C}}(t)}{dt}}{X_{\mathrm{C}}(t)} m \qquad (S13)$$

Assuming the organ's drug clearance capacity does not change over the measurement period:

$$\overline{CL} \cdot X_{\mathrm{C}}(t)dt = V_C dX_{\mathrm{C}}(t) \qquad (S14)$$

Integrating from *t* = 0 to the complete clearance of the drug yields:

$$\overline{CL} \cdot A\mathrm{UC}_{\mathrm{C}} = m_0 \qquad (S15)$$

Thus, the average drug clearance is:

$$\overline{CL} = \frac{m_0}{\left(\frac{A}{\alpha} + \frac{B}{\beta}\right)} = \frac{\epsilon U\, m_0\alpha\beta}{Z(\alpha-\beta)} = \frac{U^{*}m_0\alpha\beta}{Z(\alpha-\beta)} \qquad (S16)$$

Reaction kinetic analysis of dealloying mechanisms

In the following section, we present a kinetic analysis of the chemical dealloying process and compare it with our electrochemical stress mitigated dealloying (SMD) method. Although slowing down chemical dealloying by reducing temperature or etchant concentration is theoretically feasible, this strategy suffers from significant practical limitations, including poor control over surface quality, narrow tunable range, limited precision, and increased operational cost.

1. Thermodynamic and kinetic basis

From a thermodynamic standpoint, the dissolution of silver in nitric acid follows the overall redox reaction:

$$\mathrm{Ag} + \mathrm{HNO_3} \rightarrow \mathrm{Ag^+} + \mathrm{NO}_x$$

where x can be 1 or 2 depending on the nitric acid concentration. The overall reaction rate is governed by both nitric acid concentration and temperature.

2. Nitric acid concentration dependence

The rate as a function of nitric acid concentration follows a power law expression:

$$\text{Rate} = k_0[\text{HNO}_3]^n$$

where k_0 is the rate constant and n is the reaction order, which varies with acid concentration. Specifically:

- For high concentrations (> 6 M), $n = 0$, indicating diffusion-limited kinetics.
- For intermediate concentrations (2–6 M), $n = 1$, indicating first-order reaction kinetics.
- For low concentrations (< 2 M), $n = 2$, reflecting higher reaction sensitivity.

Since this is a solid-liquid heterogeneous reaction, the Ag^+ concentration does not directly influence the intrinsic kinetics, though product accumulation can affect diffusion gradients.

3. Temperature dependence

The temperature dependence follows the Arrhenius equation:

$$k = k_0 \exp\left(-\frac{\Delta G^{\ddagger}}{RT}\right)$$

where $\Delta G^{\ddagger} = 52$ kJ/mol is the apparent activation free energy, R is the universal gas constant, and T is the absolute temperature. Combining both dependencies, the overall rate becomes:

$$\text{Rate} = k_0[\text{HNO}_3]^n \exp\left(-\frac{\Delta G^{\ddagger}}{RT}\right)$$

4. Electrochemical stress mitigated dealloying

In our SMD process, the reaction is conducted in 50 mM H_2SO_4 without generation of NO or NO_2 gases. The rate is modulated by the applied electrochemical potential and follows the Butler-Volmer formulation:

$$\text{Rate} = k_0 \exp\left[\frac{\alpha F(E_{\text{app}} - E_{\text{eq}})}{RT}\right]$$

where E_{sp} is the applied potential, E_{eq} is the equilibrium potential, α is the charge transfer coefficient (typically ≈ 0.5), F is the Faraday constant, and T is the temperature.

5. Comparison and practical considerations

Our kinetic analysis highlights several engineering challenges with controlling the chemical dealloying process via temperature and concentration alone:

- **Nonlinear and discontinuous rate behavior:** The reaction order *n* changes abruptly (0 → 1 → 2) with dilution, leading to unpredictable shifts in etching rates.

- **Limited temperature control precision and range:** Commercial heaters typically have a precision of 1 K, which corresponds to a 5% change in reaction rate. In contrast, electrochemical potentials can be modulated with sub-millivolt precision, giving better control (e.g., a 1 mV change alters the rate by only 1.95%). The usable temperature window is narrow (typically room temperature to 85°C), whereas the electrochemical potential can be tuned over a broader range (0–1.4 V) before water hydrolysis dominates.

- **Inconsistent etching depth and morphology:** Relying on temperature or concentration alone will result in incomplete dealloying in deeper regions, or the formation of a less uniform or more defective gold network if the dissolution front is not well-controlled. The reported result also highlights how the structure of the residual gold layer and the transition between chemical and diffusion control are complex and depend on alloy composition and conditions; precise electrochemical control is better suited to navigate these complexities.

- **Environmental and safety issues:** Chemical dealloying generates toxic NO_x gases, requiring strict fume control and waste treatment. In contrast, our SMD process is environmentally benign and gas-free.

In summary, although slowing down chemical dealloying using reduced temperature or diluted etchant is theoretically feasible, this approach suffers from poor precision, limited tunability, and environmental concerns. The SMD method overcomes these limitations by enabling fine control through potential modulation.

Adhesion layer enhancement from the homogenous gold adhesion layer

The enhanced mechanical strength from the adhesion layer was calculated by:

$$\frac{\gamma_{\mathrm{Au,max}}}{\gamma_{\mathrm{Ti,max}}} = \frac{\sigma_{\mathrm{u,Ti}} \times h_{\mathrm{homogenous}}}{\sigma_{\mathrm{u,Au}} \times h_{\mathrm{heterogeneous}}} = 150$$

γ represent the maximum surface stress the structure can withstand without cracking. The estimation is based on the thickness of Ti and Au being 50 nm and 20 μm, respectively, with ultimate tensile strengths $\sigma_{\mathrm{u,Ti}}$ = 320 MPa and $\sigma_{\mathrm{u,Au}}$ = 120 MPa. The sputtering of micrometer thick Ti is also hard due to the spontaneous cracking.

Fabrication of nanoporous electrodes via conventional rushed dealloy

To form the nanoporous gold using the conventional rushed dealloy method, the dealloy is achieved by one of the following procedures: 1) performing 5 cycles of CV in 50 mM H_2SO_4 solution with a potential window of 0.2–1.35 V (versus Ag/AgCl) at a scan rate of 0.1 V/s (EC-CV); 2) performing a 300 s of amperometry at a voltage of 1.2 V (versus Ag/AgCl) in 50 mM H_2SO_4 solution (EC-IT); 3) or direct dealloy in nitric acid (68-70 wt.% in water, used as received) at 65°C for 4 minutes without electrochemical treatment (HNO_3@65°C). The temperature is maintained using hotplate (Fisher Scientific) and measured through infrared thermometers (Fisher Scientific). The electrodes were then rinsed with DI water before surface chemistry characterization or functionalization.

Fabrication of nanodendritic electrodes

The fabrication of nanodendritic electrodes was based on the needle electrodes with homogeneous gold adhesion mentioned above. To form the nanodendritic layer, the electrode was immersed in a solution containing 1.2 mg/mL chloroauric acid, 0.1 M sodium chloride and 1.5% wt. hydrochloric acid. A pulsed waveform cycle between 0 and -0.4 V was applied to the electrode for 240 cycles with a holding time of 1 s at each potential.

Electrode electrochemistry characterization

All potential reported below is vs. Ag/AgCl. To measure the potential window, nanoporous gold electrodes fabricated from SMD with different adhesion layer were placed in an electrochemical cell (counter electrode: platinum) containing 30 mL PBS. The CV was performed with a potential range from -1.2 V to 1.35 V at a scan rate of 50 mV/s. The potential window range is defined by a threshold current density of 3 mA/cm^2, the area here refers to the physical dimension.

The corrosion and corresponding ECSA monitoring were performed in the same electrochemical cell as predescribed for potential window measurement. The gold electrodes were held under a constant +0.5 V. To measure the ECSA, a series of CV were performed during certain time point intervals (from 0 to 42 hours) with different scan rates (-50 to 0 mV; 15, 60, 100, 200 mV/s). For each time point, a linear fitting for current at -25 mV versus different scan rates was done and the slope was taken and calculated as ECSA (assume 20 μF/cm^2). The whole process was programmed using homemade MATLAB code.

To assess the quality of various nanoporous electrodes, voltammetry tests were conducted in a 50 mM H_2SO_4 solution to facilitate the gold surface oxidation. The testing parameters were set from 0.2 to 1.35 V at a scan rate of 100 mV/s using the aforementioned three-electrode setup.

To investigate the impact of Knudsen diffusion on the electron transfer dynamics of RNB, CV experiments were conducted at various scan rates (0.02, 0.05, 0.1, 0.2, 0.4, 0.8 V/s) using an electrochemical cell with PBS containing 500 μM methylene blue. Analysis of the "b-value" was performed by examining the corresponding voltammograms. The peak current (I_{peak}) follows a power-law relationship with the scan rate (v), represented by the equation:

$$I_{peak} = a * v^b$$

where a and b are constants. The dimensionless b-value is determined by performing linear regression on the logarithmic values of I_{peak} versus v and calculating the slope.

To monitor the dealloying progress, an electrochemical quartz crystal microbalance (EQCM, Model 10M, Gamry) was used to record the electrode mass change. Au-coated AT-cut quartz crystals were used as the substrate, which were initially calibrated with a frequency constant of 56.6 MHz. The working electrode was then sputtered with 10 nm Ti and 60 nm Au/Ag (ratio 1:2) with an exposed area of 1.1 cm^2. The electrode setup included a platinum counter electrode and an Ag/AgCl reference electrode and was dealloyed by different methods. The mass change was calculated by converting the frequency change using the Sauerbrey equation:

$$\Delta m = -C_f \times \Delta f$$

where Δm is the mass change, C_f is the calibration constant, and Δf is the frequency change. The corresponding dealloy progress is defined as:

$$\text{Dealloy Progress (\%)} = \left(1 - \frac{\Delta m}{M_0}\right) \times 100$$

RuHex chronocoulometric determination of aptamer probe density

The sensors were equilibrated in 10 mM Tris (pH 7.4) and subjected to a potential step from +0.10 V to –0.40 V (vs Ag/AgCl) before and after introducing 50 µM hexaammineruthenium(III) chloride (RuHex). In low-ionic-strength media, RuHex binds DNA phosphates in a 1:3 stoichiometry, enabling coulometric counting of surface-bound strands.

The chronocoulometric response follows:

$$Q(t) = B\, t^{1/2} + Q_{\mathrm{dl}} + \Delta Q_{\mathrm{RuHex}}$$

where $\Delta Q_{\mathrm{RuHex}}$ is the intercept difference of the linear Q–$t^{1/2}$ plots. Aptamer surface density is obtained from:

$$\Gamma_{\mathrm{aptamer}} = \frac{\Delta Q_{\mathrm{RuHex}}}{nFA}\left(\frac{z}{m}\right) N_A,$$

with n = 1 (electrons per RuHex), F is Faraday constant, A electrode area (from cyclic voltammetry), z = 3 (binding ratio), m = 45 (bases), and N_A Avogadro's number.

Electrochemical impedance spectroscopy (EIS) and charge transfer analysis

For EIS and charge transfer analysis, first, a 10 Hz SWV was performed to capture the peak current position for reduction potential (Ered) in the respective test solution. Then EIS was performed at the Ered with an AC waveform of 10 mV amplitude and frequency ranging from 1 Hz to 100000 Hz. The result Bode plot was fitted with a corrected Randles circuit model using constant phase elements.

Sensor electrochemical characterization

The aptamer sensors were interrogated using SWV (-0.1 to -0.45 V vs. Ag/AgCl; increment: 1 mV, pulse amplitude: 25 mV) with varied frequency. The voltammograms were processed to extract peak current information after the series addition of the target analyte. The dissociation constate (K_d) is quantified by fitting the calibration curve into Langmuir adsorption model:

$$\text{Sensor response} \propto \frac{\mathrm{c[Analyte]}}{\mathrm{c[Analyte]} + \mathrm{K_d}}$$

To characterize the fouling performance of the sensor, different vancomycin sensing electrodes (RNB, planar gold-disc, and nanodendritic) were placed in UV-sterilized electrochemical cells containing fetal bovine serum and enclosed with parafilm and aluminum foil. Continuous SWV measurements were carried out every 10 minutes for up to 9 days.

Molecular pendulum sensor fabrication

To fabricate molecular pendulum sensor for BNP, two aptamer sequences were used:

P1: 5′-/5ThioMC6-D/TACCAGCTATTGTATCTAATAAGA/3FerrK/-3′,

P2: 5′-
GGCGATTCGTGATCTCTGCTCTCGGTTTCGCGTTCGTTCGTTTTCTTATTAGATA

CAATAGCTGGTA-3’

2 µL of P1 was reduced with 6 µL PBS and 2 µL of 100 µM TCEP for 1 hour in the dark. The solution was then heated at 55 °C for 5 minutes and chilled for 5 minutes. 1.8 µL of a 1 mM MCH solution was added to passivate the metal surface. The solution was combined with 4µL of 100µM P2 and rested for 10 minutes for the hybridization. The RNB was then incubated in the solution, sealed with parafilm to prevent any contaminating reaction with the air, and incubated overnight at room temperature before use.

Lactate and pH sensor fabrication

To fabricate RNB-based lactate sensors, platinum (Pt) was electrochemically deposited onto the electrode by chronoamperometry at -0.1V (vs. Ag/AgCl) for 10 min in a fresh Pt solution containing 2.5 mM H_2PtCl_6 and 1.5 mM formic acid. Then lactate oxidase was electrochemically deposited on the needle by applying a +0.6 V (vs. Ag/AgCl) for 5 min in a solution containing 2.5 mg/mL enzyme and 1 mM o-Phenylenediamine. Finally, 2 µL of 0.3 % wt. PVC was coated 3 times as diffusion-limiting layer.

The pH sensor was fabricated through the electrochemical deposition of Pt and iridium oxide on RNB. Initially, Pt was deposited onto the electrodes using chronoamperometry at -0.1V (vs. Ag/AgCl) for 10 minutes in a solution containing 2.5 mM H_2PtCl_6 and 1.5 mM formic acid. For the iridium oxide deposition, the precursor solution was prepared by dissolving 45 mg of iridium

(IV) chloride hydrate in 30 mL of DI water, followed by the addition of 300 microliters of H_2O_2 and 150 mg of oxalic acid dihydrate. The pH was then adjusted to approximately 10.5 using a 1 M sodium hydroxide solution. This iridium oxide precursor solution was left to stabilize for two days. Iridium oxide (IrOx) was then deposited onto the electrodes using CV, conducted over 200 segments with a potential range from 0 to 0.6 V (vs. Ag/AgCl) at a scan rate of 0.05 V/s. Following deposition, the electrodes were thoroughly rinsed with HPLC water to remove any residual chemicals and were then prepared for further testing or integration.

ICP-MS quantification of Au debris in artificial tissue

To quantify the Au residue of nanodendritic and RNB after the artificial tissue insertion test, inductively coupled plasma mass spectrometry (ICP-MS) was employed to detect trace amounts of Au remaining within the AT. Each AT group underwent digestion in 1 mL of aqua regia at 30°C, followed by a 500-fold dilution with a 2% nitric acid solution. For calibration, a standard 1 µg/mL Au solution in hydrochloric acid was diluted to final concentrations of 1, 10, 50, and 100 ng/mL using 2% nitric acid. The analysis was conducted using an 8800 ICP-MS Triple Quad system (Agilent Technologies) equipped with an SPS 4 Autosampler. Measurements were performed in no-gas mode with yttrium (Y) as the internal standard (IS). Key instrument settings included an RF power of 1550 W, RF matching of 1.8 V, a sample depth of 8 mm, a carrier gas flow rate of 0.9 L/min, a nebulizer pump rate of 0.1 rps, and an S/C temperature of 2°C. The gas switch was set to a dilution gas flow rate of 0.2 L/min.

Artificial tissue fabrication and insertion experiment

To mimic the different stiffness of tissues, 10, 5, 2, 1, 0.5, and 0.2 wt.% of agarose hydrogel gel were made for the insertion test by mixing with HPLC water and heated to 80 °C for 20 minutes before being cured in predefined 3D printed mold. The as-fabricated vancomycin microneedle-based sensors with different nanostructures (*i.e.*, RNB and nanodendritic electrodes) were inserted inside the gel. After each time of insertion, the sensors were scanned with the SWV technique to determine the remaining percentage of the signal. More specifically, 1, 3, 5, and 10 accumulated times insertion were performed in order and scanned with SWV for each step. To quantify the modulus of AT, the sample underwent a standard compression test, and Young's modulus was quantified according to the stress-strain data obtained during testing, utilizing the slope of the linear elastic region of the stress-strain curve.

Mechanical Finite Element Analysis

1. Geometry and Physical Modeling

Finite element simulations were performed using the Fluid-Structure Interaction (FSI) module in COMSOL Multiphysics 6.0 to investigate the influence of lateral flow on nanostructures. The three-dimensional model consisted of two distinct domains: a solid domain and a surrounding fluid domain. The solid domain included a cuboidal base with either an extruded cylindrical feature (representing an extroverted nanodendritic structure) or a cylindrical recess (representing an introverted nanoporous feature). The height/depth of the cylinder ranged from 0.05 to 33.3, and its diameter varied from 0.03 to 1 µm.

2. Material Properties:

The solid domain was modeled as gold with linear elastic behavior, using a Young's modulus of $E = 76$ GPa, a density of $\rho = 19.3$ g/cm^3, and a Poisson's ratio of $\nu = 0.442$. The fluid domain was defined with a density of $\rho = 1$ g/cm^3 and a dynamic viscosity ranging from 1 to 100 mPa·s.

3. Boundary Conditions

A fixed constraint was applied to the bottom surface of the solid domain. The lateral (left and right) faces had roller boundary conditions, while the front and back faces were treated as symmetry planes. In the fluid domain, a fully developed laminar flow was introduced from the left inlet at average velocities ranging from 0.01 to 0.0001 m/s. The right outlet was assigned a pressure boundary condition, while the front and back faces were symmetric and the top boundary was left open. The fluid and structural domains were fully coupled using the FSI module to capture the interaction between flow and deformation.

4. Mesh Generation

A physics-controlled mesh with fine resolution was used across all simulations. Element types included tetrahedra, triangles, prisms, pyramids, and quadrilaterals. The total number of mesh elements varied depending on the geometry of the nanostructure.

5. Postprocessing and Stress Analysis

Surface stresses were evaluated using the equivalent (von Mises) stress, defined as:

$$\boldsymbol{\sigma}_{\mathbf{vm}} = \sqrt{\frac{\mathbf{1}}{\mathbf{2}}[(\boldsymbol{\sigma}_{\mathbf{1}} - \boldsymbol{\sigma}_{\mathbf{2}})^{\mathbf{2}} + (\boldsymbol{\sigma}_{\mathbf{2}} - \boldsymbol{\sigma}_{\mathbf{3}})^{\mathbf{2}} + (\boldsymbol{\sigma}_{\mathbf{3}} - \boldsymbol{\sigma}_{\mathbf{1}})^{\mathbf{2}}]} \qquad (\boldsymbol{S}\mathbf{17})$$

where σ_1, σ_2, and σ_3 are the principal stresses. Yielding is predicted when σ_{VM} exceeds the yield strength of the material.

To assess stress concentration, the stress concentration ratio $\boldsymbol{\eta}$ was computed as:

$$\boldsymbol{\eta} = \frac{\boldsymbol{\sigma}_{\mathbf{max}}}{\boldsymbol{\sigma}_{\mathbf{load}}} \qquad (\boldsymbol{S}\mathbf{18})$$

where σ_{load} is the average applied stress and σ_{max} is the maximum local stress within the structure.

Ex vivo multi-organs and in vivo tumor vancomycin test

The brain, lung, kidney, liver, and biceps femoris tissues were collected from freshly euthanized, healthy Sprague-Dawley rats. Fresh bovine tendon was sourced from a local grocery store in Los Angeles, California. Solid tumor tissue culture procedures were conducted under protocols approved by the Institutional Animal Care and Use Committee at the University of California, Los Angeles (Protocol R-17-072). Female C57BL/6J mice (The Jackson Laboratory, Strain #000664), aged 8 weeks, were each injected subcutaneously on both dorsal flanks with 0.5 million murine colon adenocarcinoma cells (ATCC, MC-38). Fourteen days post-injection, the mice were euthanized, and tumor tissues were collected. Each type of organ (brain, kidney, liver, tumor, lung, biceps femoris, and bovine tendon) was soaked under 0, 10, 20, and 40 µM of vancomycin solution overnight. Then the packed microneedle sensors were inserted on the surface of each organ. To ensure the needle-organ contact area is dry, the surface of each organ was gently wiped prior to the test.

To assess the RNB vancomycin sensor in tumor tissue, we applied a microneedle device in murine subcutaneous tumor models (MC-38) mentioned above in a mouse under anesthesia. The tumor is about 200 µm under the skin. The SWV was carried out at a frequency of 25 Hz and 150 Hz. The mouse was then administered with 30 mg/kg of vancomycin via retro-orbital injections. The mouse was euthanized after the experiment.

Wireless TDM device integration

The wireless TDM device consists of three parts: 1) microneedle three-electrode sensing interface patch. The patch consists of three electrodes: counter, reference, and working, which are fixed in a PDMS substrate. The counter electrode was prepared by coating the needle electrode with a layer of homogeneous adhesion as previously described. The needle-based reference electrode originated from the lancet needle and was dip-coated with Ag/AgCl ink (50% diluted with toluene). The three electrodes were planted into the PDMS that was reverse molded into the PLA 3D-printed case. 2) a flexible circuit. The wireless miniaturized electrochemical potentiostat was realized based on a FPCB. A microcontroller unit (MCU) (Atmega328 U-TH) is programmed to generate the square waveform and read the sensor's current at the appropriate interval. In particular, the MCU controls a dual-channel digital-analog converter (DAC) (DAC8552; Texas Instruments) with SPI commands to modulate the voltage difference across the reference and working electrode. The working electrode is connected at the negative terminal of a transimpedance amplifier (TIA), which translates the current across the sensor into a voltage difference measured by an analog-digital converter (ADS1256; Texas Instruments). As the experiment occurs, the raw difference current for each cathodic electrical pulse (the y-axis, of a voltammogram) is streamed over the serial connection to an onboard Bluetooth module (Proteus-III; Wurth Eletronik). On the connected client, the raw difference current can be processed with a Butterworth and moving average filter to produce a smooth voltammogram. 3) auxiliary components such as a lithium battery (110 mAh) for powering and a 3D printed case for packaging, along with a biocompatible adhesion layer (Tegaderm film or double-sided tape, 3M Science) to provide robust attachment to the skin.

Biocompatibility test

To evaluate the cytotoxicity of the RNB, human dermal fibroblasts (HDFs) were seeded and cultured directly on the electrode surface using Dulbecco's modified eagle medium (Gibco) supplemented with 10% fetal bovine serum for 48 hours. Subsequently, the cells were stained with live (calcein-AM) or dead (ethidium homodimer-1) reagent, allowing the evaluation of cell viability through fluorescence microscopy. For the long-term biocompatibility study of the RNB, the electrodes were incubated in Dulbecco's modified eagle medium (Gibco) at 37°C in a 5% CO_2 incubator for 7 days. A positive control was established by incorporating $AgNO_3$ into the medium to achieve a final concentration of 10 µg/mL. HDFs were then cultured in this conditioned medium supplement with 10% fetal bovine serum for 72 hours. Cell viability was assessed at 24 hours and 72 hours using PrestoBlue cell viability staining reagent, followed by fluorescence quantification (excitation wavelength 560 nm, emission wavelength 590 nm).

In vivo vancomycin sensing and CKD monitoring

The experiment to measure vancomycin TDM is similar to the above experiment, but the sensor was removed after each TDM session. Besides the same pre-administration blood collection, the blood samples were intermittently collected through the femoral vein during sensor monitoring for LC-MS quantification. For vancomycin TDM experiment in rats with compromised kidney function: this experiment replaces the general daily diet with a high adenine diet. The adenine diet was prepared by mixing powdered adenine with rat food pellets (Teklad 7013), resulting in a concentration of 0.75% by weight. One group of rats ($n = 3$) were fed with the high adenine diet for up to 7 weeks. The blood work was done every 7 days and if they showed symptoms of pain or distress, the analgesics (meloxicam or ibuprofen) would be administered orally daily. During the 7 weeks of diet, the continuous vancomycin TDM experiment was performed every 7 days for each rat with a fixed dosage of 20 mg/kg unless they were diagnosed unsuitable for the procedure according to the National Institute of Health guidelines. Another rat was fed with the high adenine diet for two weeks, followed by a switch to a regular non-adenine diet and daily oral administration of allopurinol (25 mg/kg) for another two weeks. During the 4-week dietary regimen, the continuous vancomycin TDM experiment was performed every 7 days for each rat, utilizing the same fixed dosage of 20 mg/kg.

Pathological analysis

To perform the histopathology analysis on the rat with CCl_4 injection, the rat's liver was harvested 24 hours post-injection and fixed in 10% formalin solution for 72 hours. The fixed kidney was paraffin-embedded and sectioned. Section (4 µm in thickness) was collected every 20 µm throughout the sample and stained with H&E and optical photos were taken under the microscope. To perform the histopathology analysis on the rat with a high adenine diet, three rats were fed with a high adenine diet for 2, 4, and 6 weeks, and one control healthy rat, respectively, and the kidney kidneys were harvested and fixed in 10% formalin solution for 72 hours. The fixed kidney was paraffin-embedded and sectioned. Section (4 μm in thickness) was collected every 20 μm throughout the sample and stained with H&E and optical photos were taken under the microscope.

LC-MS/MS serum vancomycin analysis

Rat serum samples were analyzed using liquid chromatography with tandem mass spectrometry (LC-MS/MS) in multiple reaction monitoring (MRM) modes for vancomycin quantification, using Tobramycin as the internal standard. The protocol is adapted from our previous publication(*25*). Calibration samples were prepared by diluting vancomycin into concentrations of 2, 4, 12, and 20 μg/ml with HPLC water. To each tube containing 50 μL of these solutions, 3.2 μL of blank serum and 1.059 μL of tobramycin (1.02 mg/ml) were added. Then, 212 μL of acetonitrile was added for protein precipitation. After vortexing for 20 seconds and centrifuging at 8000 rcf for 10 minutes, 10 μL of the supernatant was transferred into 70 μL of 0.1% formic acid, mixed gently, and prepared for LC-MS/MS analysis. For serum sample analysis, 3 μL of each serum sample was mixed with 47 μL of DI water and 1 μL of tobramycin (1.02 mg/ml). This was followed by adding 200 μL of acetonitrile, and the samples underwent the same preparation steps as the calibration samples. For high-performance LC (HPLC) analysis, we used an Agilent 1200 series HPLC system (Agilent Technologies) with an HTS PAL autosampler (CTC Analytics) connected to an API 4000 triple quadrupole mass spectrometer (Sciex). The mobile phases, A (water with 0.1% formic acid) and B (acetonitrile with 0.1% formic acid) were pumped at a flow rate of 350 μL/min, with a 4-minute equilibration before sample injection. The gradient began with 5% B for 0.5 minutes, ramped up to 90% B over 3 minutes, held at 90% for 1 minute, then dropped back to 5% over 0.5 minutes and maintained at 5% for an additional 2 minutes. A 20-μL sample was loaded into the chamber using an autosampler tray. The mass spectrometer operated in MRM mode to measure specific mass-to-charge transitions: 725.5 to 144.1 for vancomycin and 468.3 to 163.2 for tobramycin. The optimized settings for vancomycin were a declustering potential of 56 V, entrance potential of 10 V, collision energy of 23 V, and collision cell exit potential of 10 V. For tobramycin, settings were a declustering potential of 76 V, entrance potential of 10 V, collision energy of 33 V, and collision cell exit potential of 10 V.

RNB cost analysis

The materials cost analysis is based on the components and equipment required to fabricate a single RNB sensor. For the homogeneous gold layer, we verified that 20 mL of gold deposition solution is sufficient for five batches of needles, with each batch comprising 16 microneedles bound together. A single co-sputtering session can deposit gold/gold-silver alloy onto an 8-inch wafer that hold approximately 800 microneedles, consuming roughly 1 gram of gold and 2 hours of machine time. The aptamer cost is calculated based on the requirement of 25 μL of reduced aptamer solution per microneedle, which is necessary to facilitate self-assembly during the incubation step. The tabular cost is shown in Table S1 below.

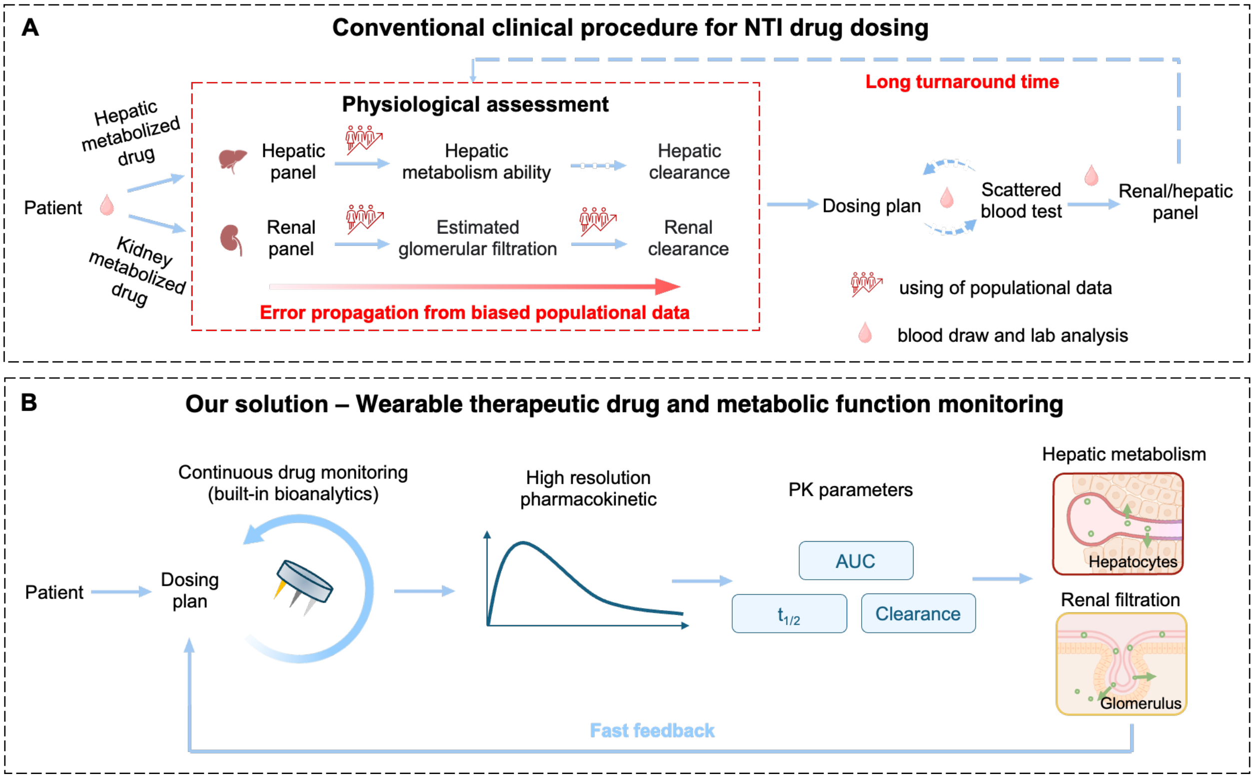

Fig. S1. Comparison between conventional blood-based therapeutic drug monitoring and wearable ISF-based therapeutic drug and metabolic function monitoring. A Conventional drug monitoring relies on blood-based methods to assess a patient's hepatic and renal function using population-level data. Physiological blood tests, such as hepatic and renal panels, estimate hepatic metabolism and glomerular filtration capabilities, which are then used to predict hepatic and renal clearance for drugs metabolized in the liver and kidneys, respectively. However, this blood-based bioanalysis workflow fails to capture the dynamic aspects of rapidly changing patient conditions, particularly in critically ill patients. Furthermore, this approach often results in errors from biased population data that overlook diverse demographic and genetic backgrounds, particularly in underrepresented groups, with inaccuracies propagate as such data are repeatedly used along the process. Furthermore, there is no unified index for hepatic clearance due to its diversity in enzymatic metabolite pathways. After these physiological assessments, a dosing plan is formulated. However, the turnaround time for it is lengthy due to scattered blood data points collected intermittently through blood draws and lab analyses. This delay in data collection and analysis results in a prolonged intervention period based on the patient's actual metabolic response. **B**, Wearable microneedle ISF-based drug monitoring approach presented in this study addresses these challenges by enabling continuous, high-resolution therapeutic drug monitoring in ISF. This ISF-based method provides a minimally invasive alternative that circumvents the need for frequent blood draws. It allows real-time measurements of key PK parameters, such as AUC, half-life, and drug clearance (*CL*) for faster and accurate organ metabolism assessment and personalized dosing.

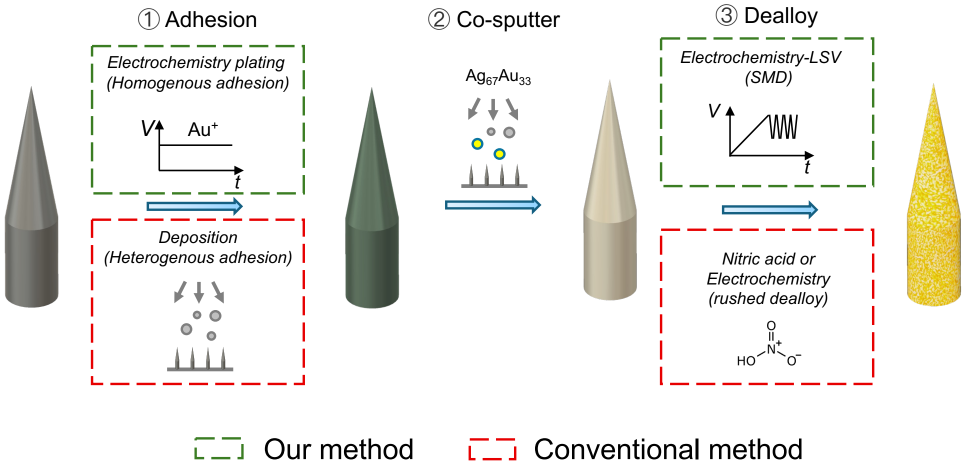

Fig. S2. Fabrication process comparison between our method and conventional methods for gold nanoporous. Detailed fabrication flow chart for microneedle-shaped RNB for minimally invasive tissue access. The process begins with adhesion: our method uses electrochemical plating to create a thick homogeneous gold adhesion layer, whereas conventional methods employ heterogeneous adhesion by depositing nanometer-thick layers of materials such as Ti or Cr, which often results in reduced mechanical strength and susceptibility to surface cracking. Next, both methods involve co-sputtering silver and gold atoms ($Ag_{67}Au_{33}$) to form an alloy precursor. For dealloying, our approach leverages the SMD process, utilizing an electrochemical method that gradually increases voltage through linear sweep voltammetry (LSV) to achieve a controlled dealloying rate. This process creates a high-quality nanoporous structure while minimizing surface stress and reducing unwanted reactions. In contrast, conventional dealloying methods, such as nitric acid corrosion or rushed electrochemical dealloying, often induce higher surface stress, cracks, and structural defects, which can ultimately compromise the sensor's long-term stability.

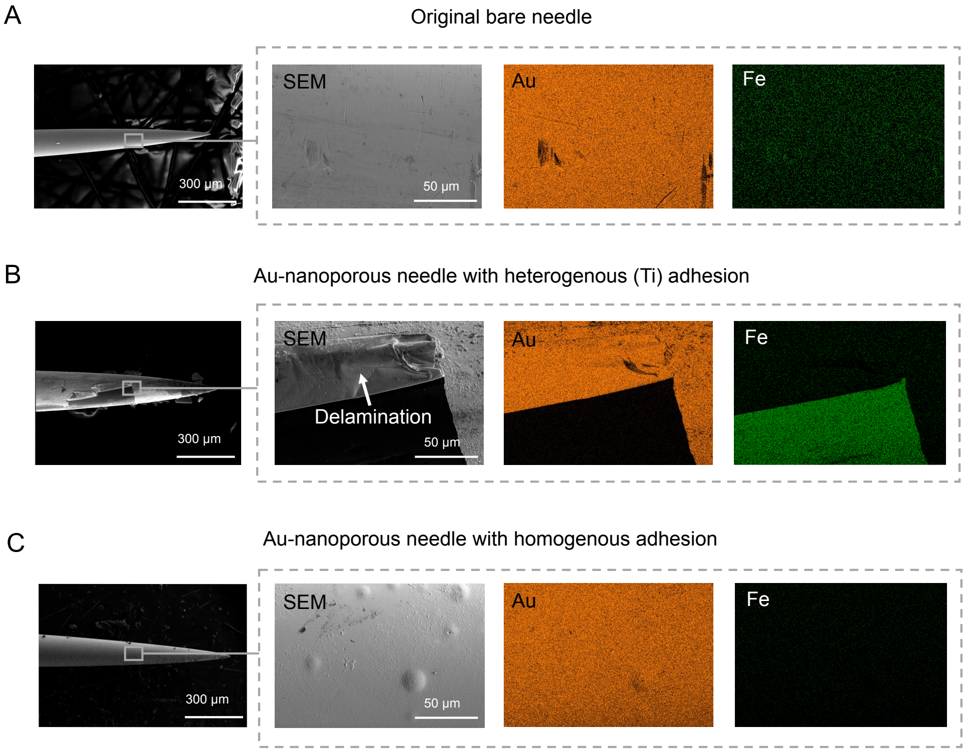

Fig. S3. Surface morphology and elemental characterization. A, Commercial bare needle. **B,** Au-nanoporous coated needle fabricated with a conventional heterogeneous Ti adhesion layer. **C,** Au-nanoporous coated needle fabricated on a homogeneous, micrometer-thick gold needle (RNB). For each sample, the panels (left to right) show: an overview of the needle surface, a higher-magnification image, EDS elemental mapping for gold (Au), and EDS mapping for iron (Fe). Samples in (**B**) and (**C**) were both dealloyed via SMD to minimize surface tension. SEM images acquired at an acceleration voltage of 10 kV.

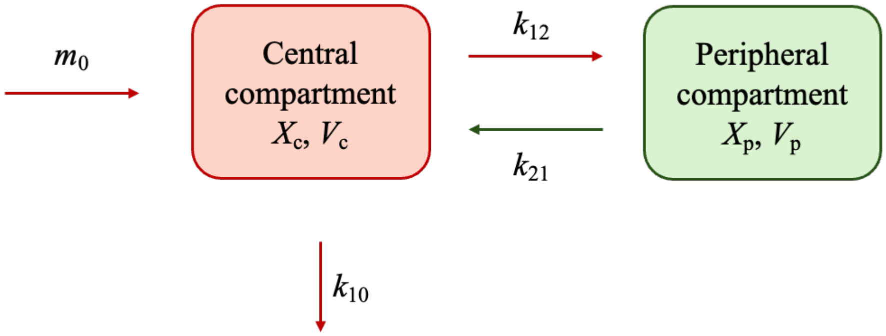

Fig. S4. Two-compartment pharmacokinetic model for peripheral monitoring. The central compartment represents the central bloodstream, while the peripheral compartment represents tissue fluids. m_0 is the total amount of drug dosed. Drug transfer between these compartments occurs via perfusion and circulation at rates k_{12} and k_{21}, with elimination at rate k_{10}. V_C and V_P are the volumes of distribution in the central and peripheral compartments, and X_C and X_P represent the drug concentrations in these compartments, respectively.

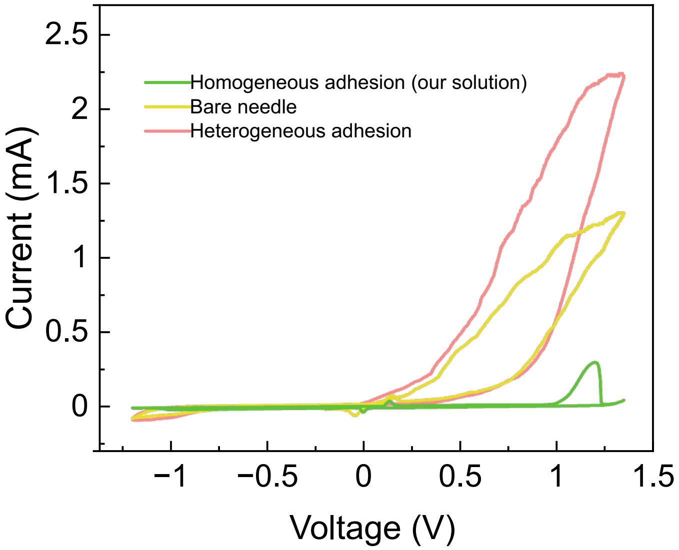

Fig. S5. Cyclic voltammetry patterns of electrode with different adhesion layers in PBS. CV profiles of electrodes with heterogeneous adhesion (50 nm Ti), bare needle, and homogeneous adhesion (our micrometer-thick gold adhesion). Experiment performed in an electrochemical cell containing phosphate buffered saline. Scan rate: 0.1 V/s, reference electrode: Ag/AgCl.

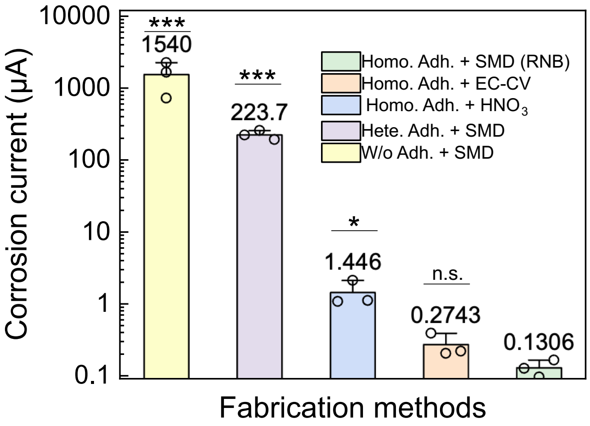

Fig. S6. Corrosion current of different nanoporous gold electrodes. The corrosion current of nanoporous gold electrodes fabricated using different methods. The electrochemical etching was performed at +0.5 V v.s. Ag/AgCl in phosphate buffered saline for 300 s. Error bars indicate standard deviation ($n = 3$). The statistical comparison is made based on RNB verses other fabrication method; "n.s.": not statistically significant, *** $P < 0.001$, * $P < 0.05$; two-tailed, two-sample t-test.

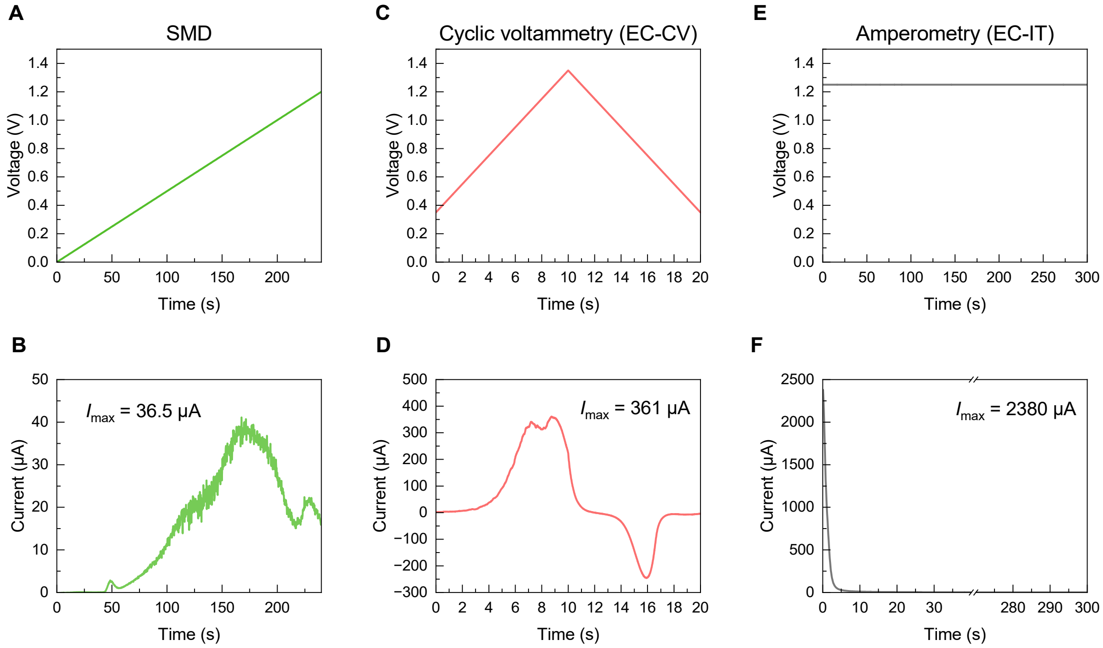

Fig. S7. Comparison of electrochemical dealloying techniques for gold nanoporous film fabrication. A-B, voltage-time (**A**) and current-time (**B**) profiles for stress mitigated dealloy (SMD) method. **C-D**, voltage-time (**C**) and current-time (**D**) profiles for EC-CV method. **E-F**, voltage-time (**E**) and current-time (**F**) profiles for electrochemistry amperometry (EC-IT) method.

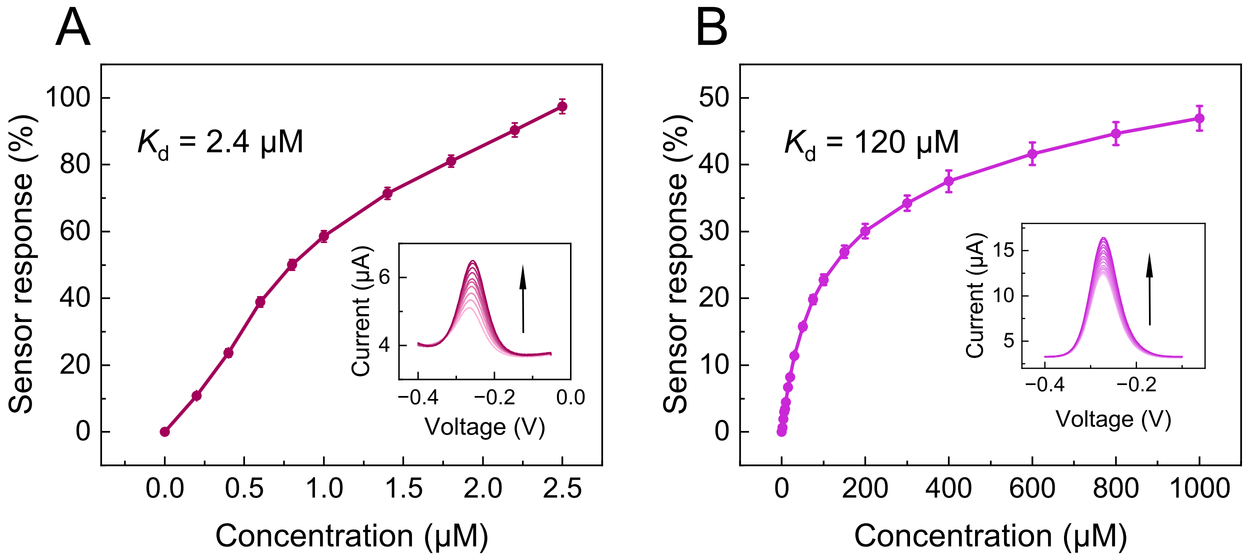

Fig. S8. Calibration curves for the Doxorubicin (A) and phenylalanine (B) aptamer sensors. Error bars indicate S.D. ($n = 3$). Insets show square wave voltammograms, with arrows indicating increasing concentration.

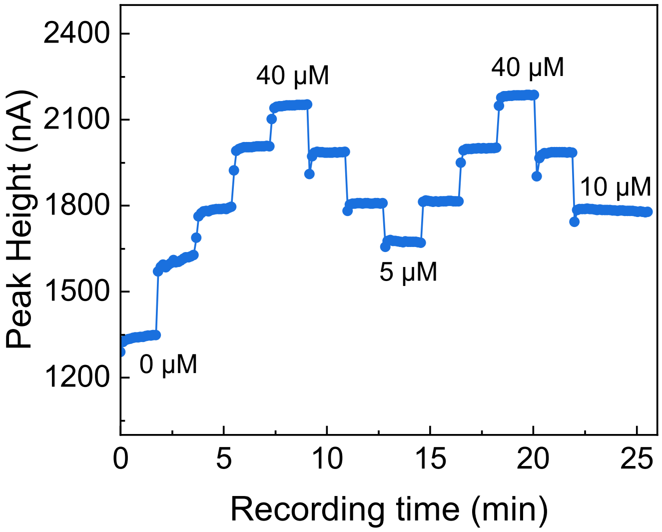

Fig. S9. Reversibility and response time of the RNB aptamer sensor. Sensor response to sequential vancomycin concentrations (5, 10, 20, and 40 µM) in PBS, demonstrating rapid and reversible signal behavior. Recording was paused during solution exchanges and resumed immediately after immersion in the new solution.

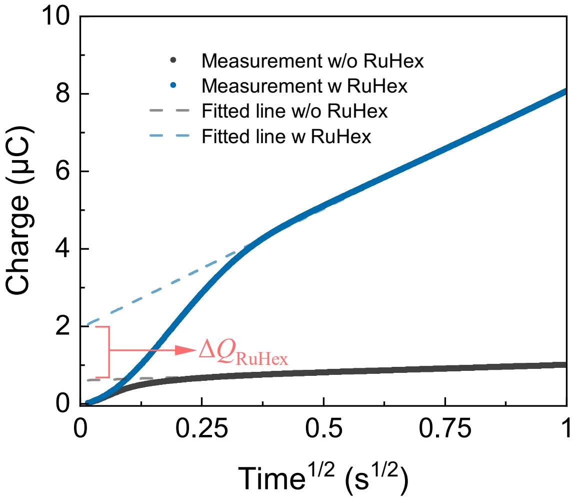

Fig. S10. Chronocoulometric quantification of aptamer density. Chronocoulometric measurements were performed on a vancomycin aptamer-functionalized RNB in 10 mM Tris buffer, before and after the addition of 50 µM RuHex. The dotted line indicates the linear fit of charge versus the square root of time for the linear part. The difference between the y-intercepts reflects the Faradaic charge contribution from RuHex bound to the immobilized aptamer.

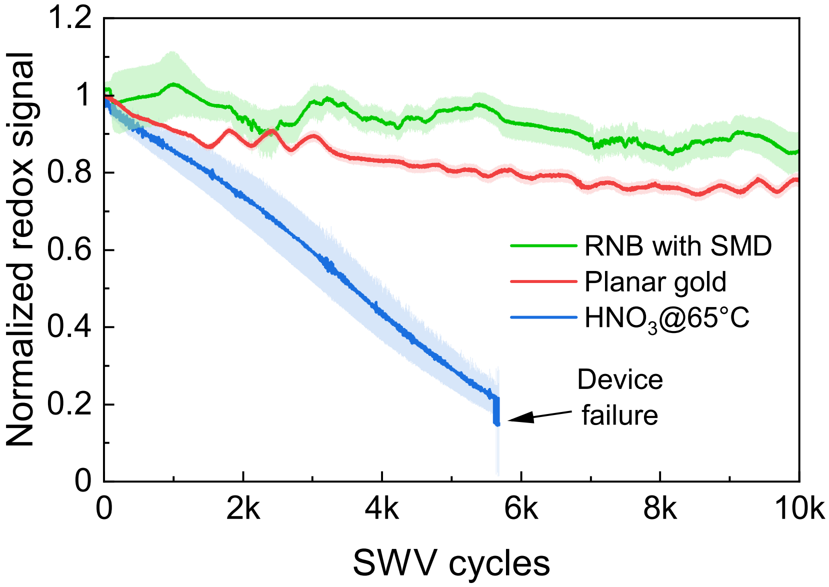

Fig. S11. Comparison of aptamer sensor redox readouts under continuous SWV. Sensors were fabricated on nanoporous gold microneedles using SMD, rushed dealloyed device at 65 °C), or standard planar gold-disc electrodes (non-nanostructured). Continuous SWV was performed at 60 Hz in PBS. Shaded areas represent standard deviation ($n = 3$). $P = 0.023$ for the comparison of number of cycles to 90% signal retention between RNB and HNO_3 treated devices. Two-tailed, two-sample *t*-tests.

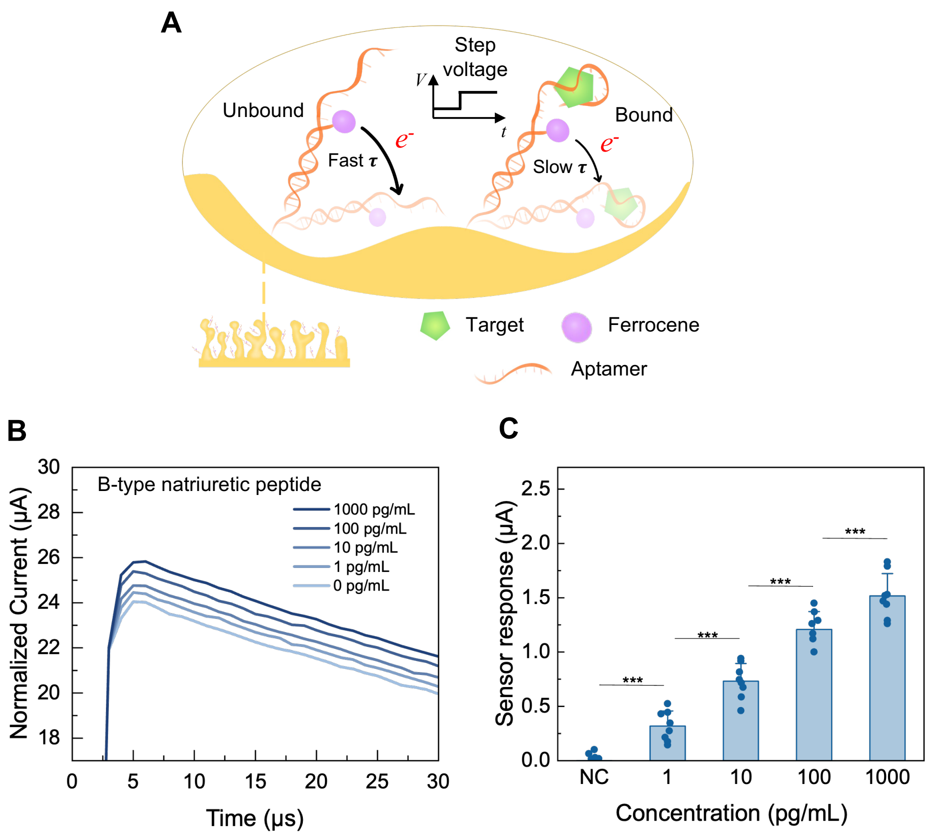

Fig. S12. Principle and performance of molecular pendulum sensor. A, Schematic of molecular pendulum sensor working principle often used for large molecules detection. The sensor consists of a rigid, negatively charged DNA linker anchored to the electrode via thiol-gold bond, with a redox reporter (*i.e.*, ferrocene)-tagged recognition aptamer (receptor) at its distal end. Upon application of a positive potential step (typically +500 mV vs Ag/AgCl), the entire construct is drawn toward the electrode by the electric field. This movement promotes electron transfer between the redox tag and the electrode, generating a measurable faradaic current. Binding of the analyte alters the hydrodynamic drag and electrostatic profile of the construct, thereby slowing the construct's approach to the electrode. This results in a measurable delay in the redox current decay, quantified by a characteristic time constant (τ). The unbound state exhibits a faster decay (shorter τ as shown in left), whereas the bound state, due to increased molecular size and drag, displays a longer τ as shown in right. **B,** Current-time profile showing the sensor response at different concentrations of BNP. The sensor operates under chronoamperometry, with a +500 mV potential step. **C,** BNP response versus at increasing concentration, showing a nonlinear increase in current as the concentration increases across a wide range (n = 8). *** represent $P < 0.001$, two-tailed, two-sample t-tests. NC denotes no concentration.

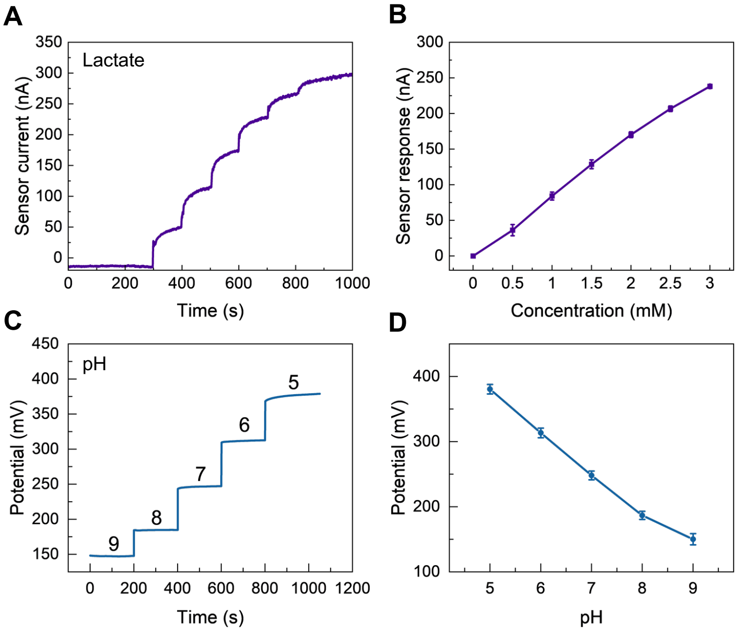

Fig. S13. Characterization of reagent-free electrochemical sensing interface on RNB. A, Current-time profile of the sensor response to increasing lactate concentrations. The electroenzymatic lactate sensor operates at +0.5 V (vs. Ag/AgCl) using amperometry. The sensor current increases in a stepwise manner as lactate concentration is adjusted every 100 seconds for 0.5 mM. **B**, Lactate calibration curve showing a linear increase in sensor response with increasing lactate concentration (*n* = 3). **C**, potential-time profile showing the sensor response at different pH conditions. The sensor operates under open-circuit potential conditions, with potential increasing in a stepwise manner as the pH changes every 200 seconds. **D**, pH calibration curve for the sensor, showing a linear decrease in potential as the pH increases across a wide range (*n* = 3).

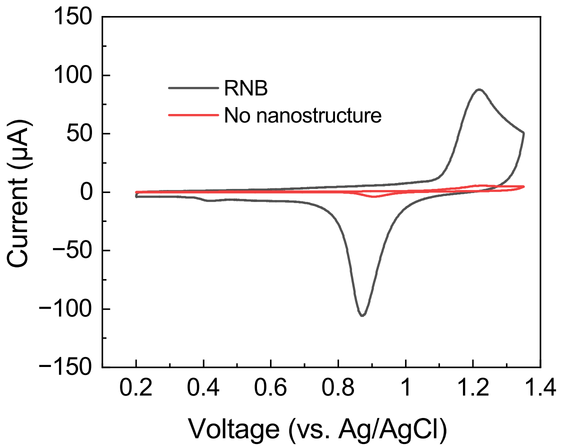

Fig. S14. Electrochemical surface area (ECSA) of electrode with homogeneous adhesion only and RNB via ORR. CV patterns in 50 mM H_2SO_4 (scan rate: 50 mV/s) showing gold oxide reduction reaction and the peak area can be used for quantification of ECSA. After nanostructured, the ECSA is enlarged 77 times compared with the original physical dimensions.

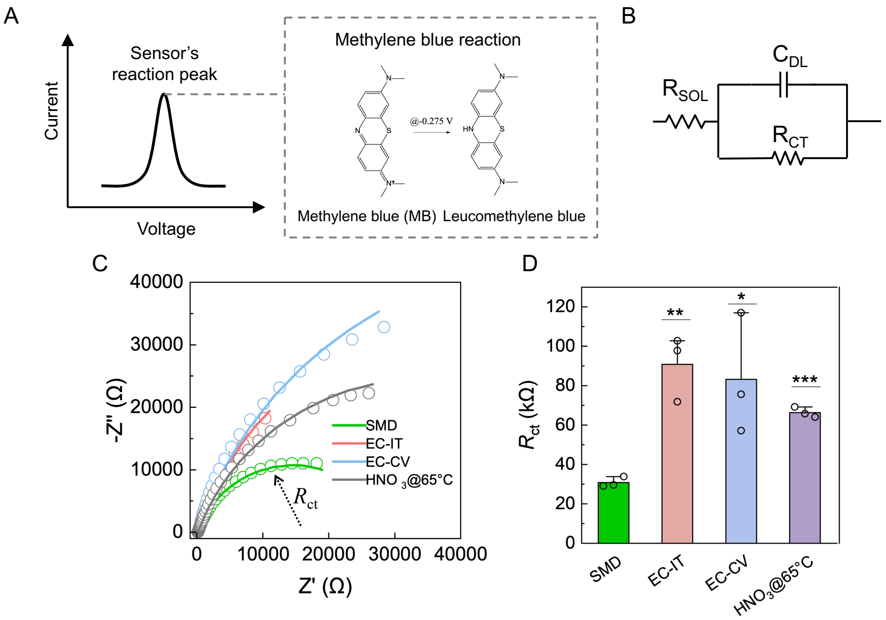

Fig. S15. Equivalent-circuit analysis of methylene-blue-mediated electron transfer. A, Origin of the sensor signal: voltametric peak generated by the reversible two-electron reduction of MB to leucomethylene blue (E_{red} = -0.275 V vs Ag/AgCl). **B,** Randles equivalent circuit used to fit the EIS data, consisting of solution resistance (R_{SOL}), double-layer capacitance (C_{DL}), and charge-transfer resistance (R_{CT}). **C,** Nyquist plots (symbols) recorded in PBS containing 500 µM freely diffusing MB for microneedles fabricated by different dealloying methods. Solid lines are least-squares fits to the circuit shown in (**B**); semicircle diameters correspond to R_{CT}. **D,** Fitted R_{CT} values (mean ± SD, $n = 3$). *** $P < 0.001$, ** $P < 0.01$, * $P < 0.05$; two-tailed, two-sample t-test verses RNB.

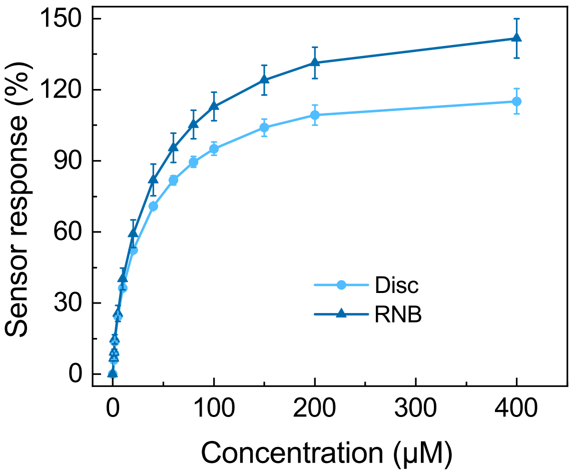

Fig. S16. Calibration curve for vancomycin aptamer sensor on RNB and disc electrode. The enhancement of the sensitivity comes from the Knudsen diffusion behavior of the target analyte. Error bars indicate S.D. (*n* = 3).

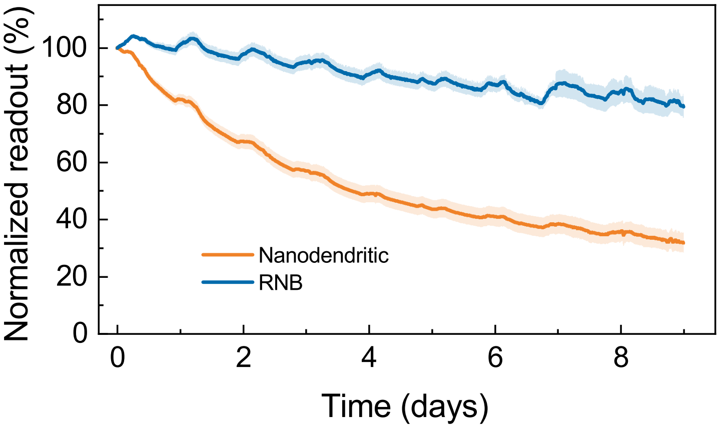

Fig. S17. Fouling performance of nanodendritic sensors. Sensor response decay in FBS for vancomycin on nanoporous and nanodendritic-based electrodes. Shaded areas represent standard deviations (*n* = 3).

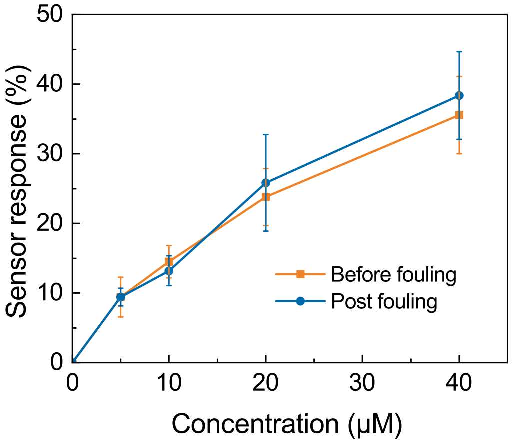

Fig. S18. Calibration curves before and after fouling. Sensor response for vancomycin before and after continuous operation in undiluted FBS for 9 days. Error bars indicate S.D. (*n* = 3).

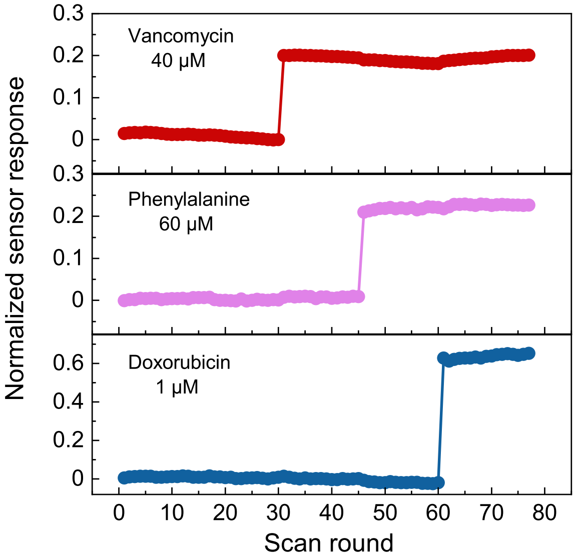

Fig. S19. Demonstration of multiplexed sensing. Three distinct sensors, each functionalized with a specific aptamer sequence, were integrated into a single PDMS-based device. Measurements were conducted using SWV at 200 Hz. Physiologically relevant concentrations of vancomycin, phenylalanine, and doxorubicin were sequentially introduced at scan rounds 30, 45, and 60, respectively.

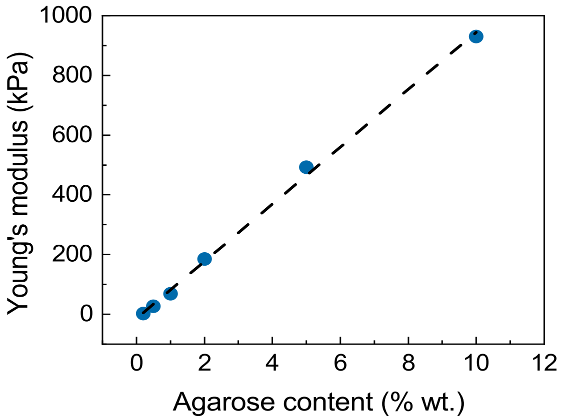

Fig. S20. Young's modulus of artificial tissues (AT) with different agarose content. The result is derived from standard compression testing and linear fitting of the elastic region.

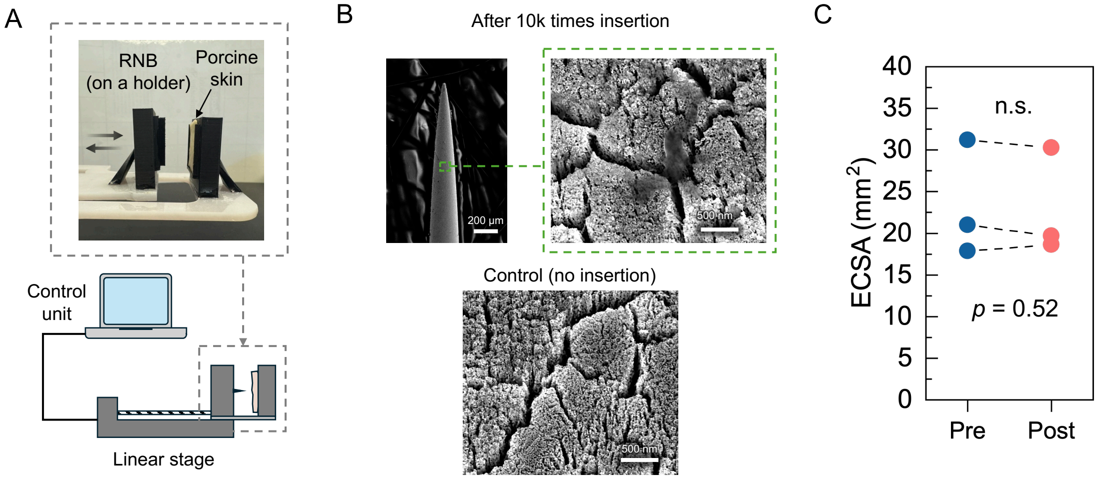

Fig. S21. Electrode robustness under repeat insertion. A, Experimental setup. **B,** SEM image of the RNB surface after 10,000 repeated insertions into porcine skin. **C,** Corresponding electrochemical surface area (ECSA) before and after insertion. “n.s.”: not statistically significant ($P > 0.05$); two-sided paired t-test ($n = 3$).

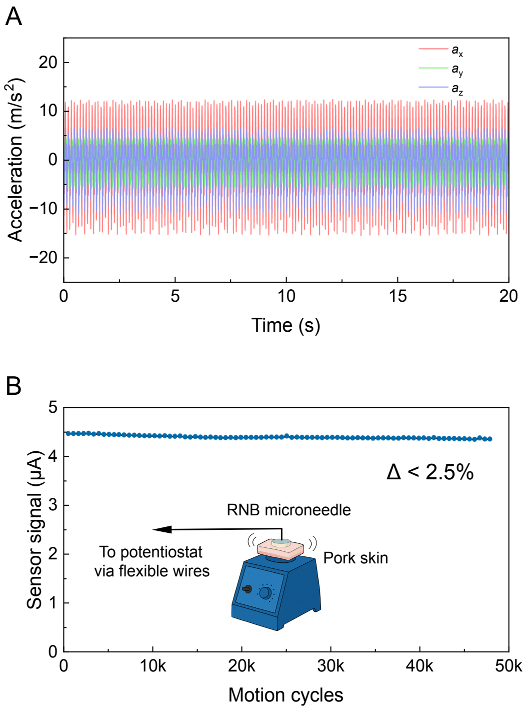

Fig. S22. RNB signal fidelity under motion. A, Sample vibrational acceleration profiles along orthogonal x, y, and z directions. **B,** Continuous readout from a vancomycin RNB microneedle patch inserted in porcine skin under 3D oscillatory acceleration. The RNB signal exhibited minimal fluctuation (< 2.5%) despite the induced motion, demonstrating robust performance under dynamic conditions.

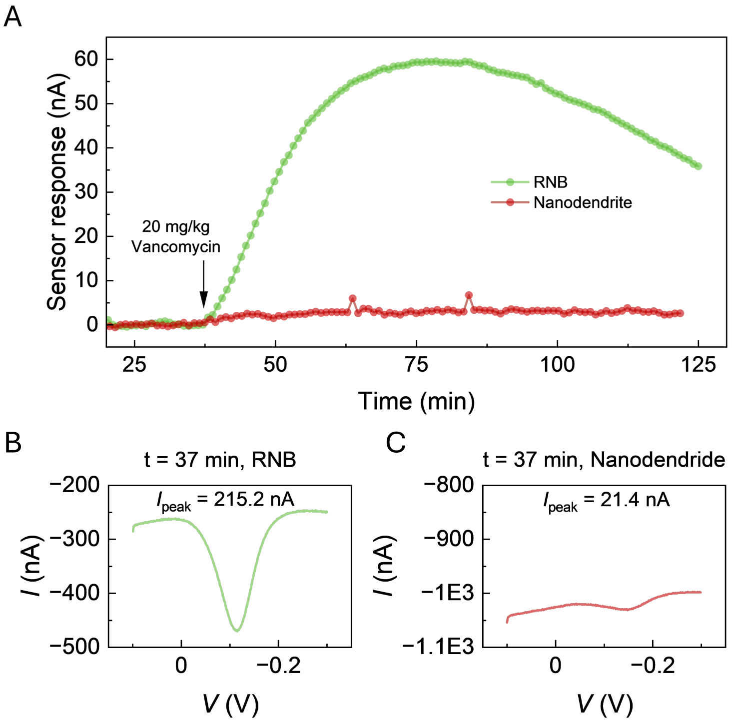

Fig. S23. ***In vivo*** **signal comparison between RNB and nanodendrite microneedle vancomycin sensor. A**, Sensors absolute current response after administration of vancomycin at $t = 37$ min. **B-C**, Raw SWV signal (150 Hz) right before the injection for RNB (**B**) and nanodendrite (**C**) microneedle sensor.

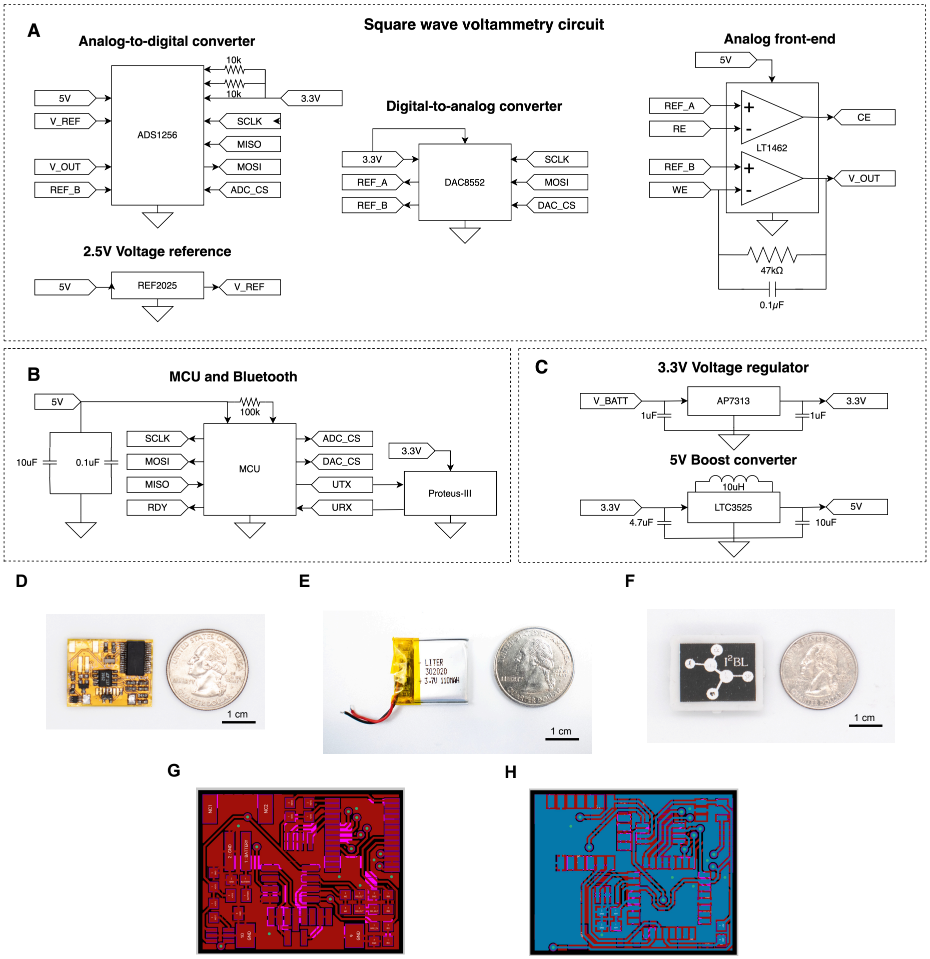

Fig. S24. Customized wireless potentiostat. A-C. Circuit schematics for the SWV module (A), microcontroller and Bluetooth module (B), and voltage regulator (C). **D-F.** Photographs of the flexible circuit (D), battery (E), and fully assembled device with optional 3D-printed case (F) shown next to a standard U.S. quarter for scale. **G-H.** Front (G) and back (H) PCB layouts of the circuit.

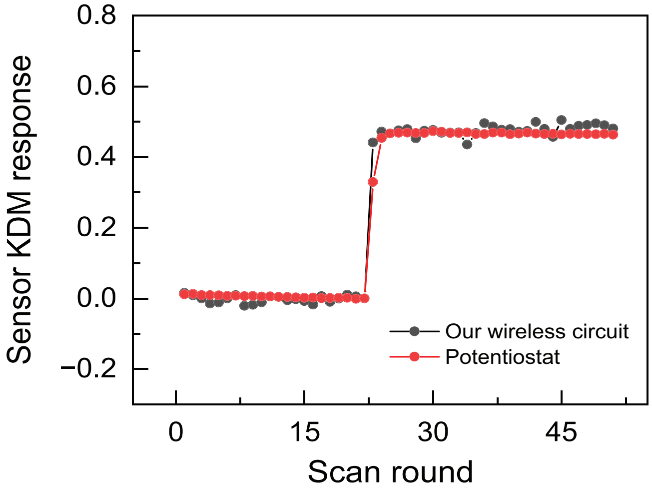

Fig. S25. Sensor response for an irinotecan sensor using our wireless circuit and a commercialized potentiostat.

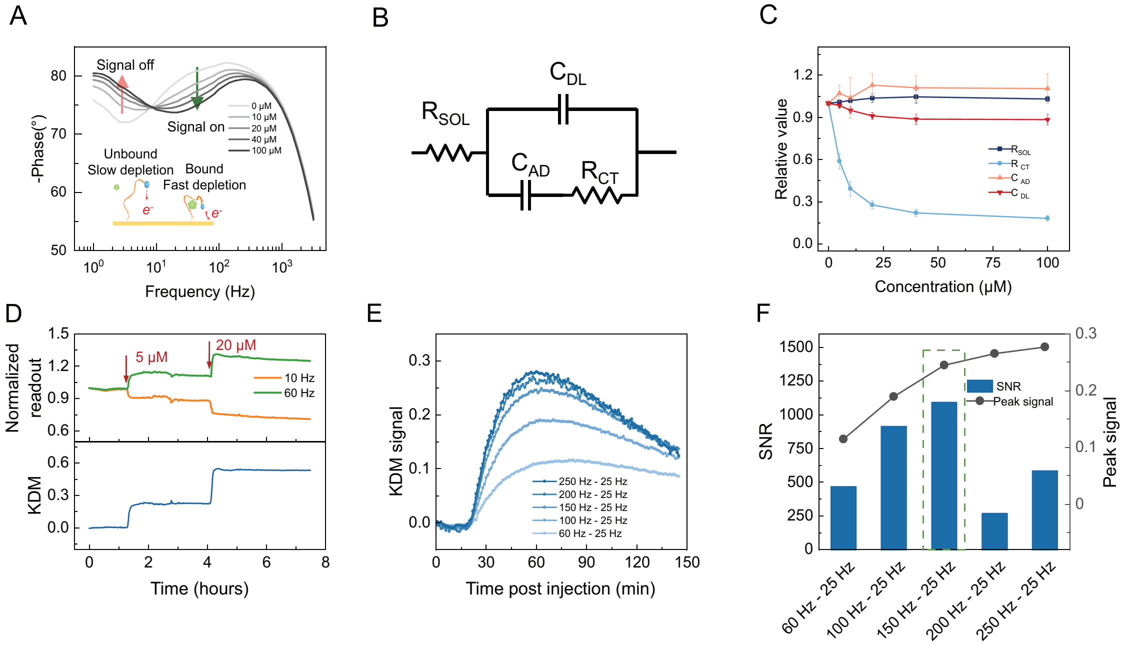

Fig. S26. Principle and performance of tissue-specific kinetic differential measurement (tKDM) for drift canceling. **A**, Phase-frequency profile shows an aptamer sensor's response to increasing vancomycin concentrations, with a phase shift observed as electron transfer from the redox reporter accelerates upon binding. The inset depicts the sensor's electrochemical process: in the unbound state, the redox reporter is distant from the electrode, resulting in slower electron transfer and extended depletion time. Upon vancomycin binding, electron transfer and redox depletion accelerate, leading to increased high-frequency currents and decreased low-frequency currents. This change manifests as a "signal-off" decrease in phase shift at low frequencies and a "signal-on" increase at high frequencies, reflecting enhanced electron transfer with binding. **B**, Equivalent circuit model of the electrochemical behavior of the EAB sensor. The circuit is modeled as a combination of resistor and capacitor components, consisting of the solution resistance (R_{SOL}) in series with the double-layer capacitance (C_{DL}). Charge-transfer resistance (R_{CT}) and pseudocapacitance (C_{AD}) are added in parallel with the double-layer capacitance due to Faradaic charge transfer. **C**, Relative value-concentration plot for different components in the equivalent circuit. As more vancomycin binds to the sensor, R_{CT} decreases, reducing the effective resistance at the interface and allowing for faster electron transfer from the redox reporter. This change in R_{CT} is the primary driver of the phase shift observed in the system, leading to the sensor's sensitivity difference across various frequencies ($n = 3$). **D**, Normalized sensor and KDM response over time in PBS solution containing 10 mg/mL bovine serum albumin. The top panel displays the sensor's stepwise response at two frequencies, 10 Hz and 60 Hz, aligning with "signal-off" and "signal-on" states, respectively, as vancomycin concentration increases from 0 to 5 μM, then to 20 μM. The bottom panel illustrates the KDM response, which enhances signal strength and mitigates drift by integrating both "signal-on" and "signal-off" responses. **E**, In vivo tKDM signal tracking over time post-injection of vancomycin (20 mg/kg) was performed using a microneedle device across various frequency combinations in a rat model. The tKDM signal initially rises following the injection, peaks, and subsequently diminishes gradually as vancomycin undergoes metabolism and elimination. Variations in frequency combinations result in distinct signal intensities as well as noise level. **F**, In vivo SNR and peak signal comparison across various frequencies used in tKDM.

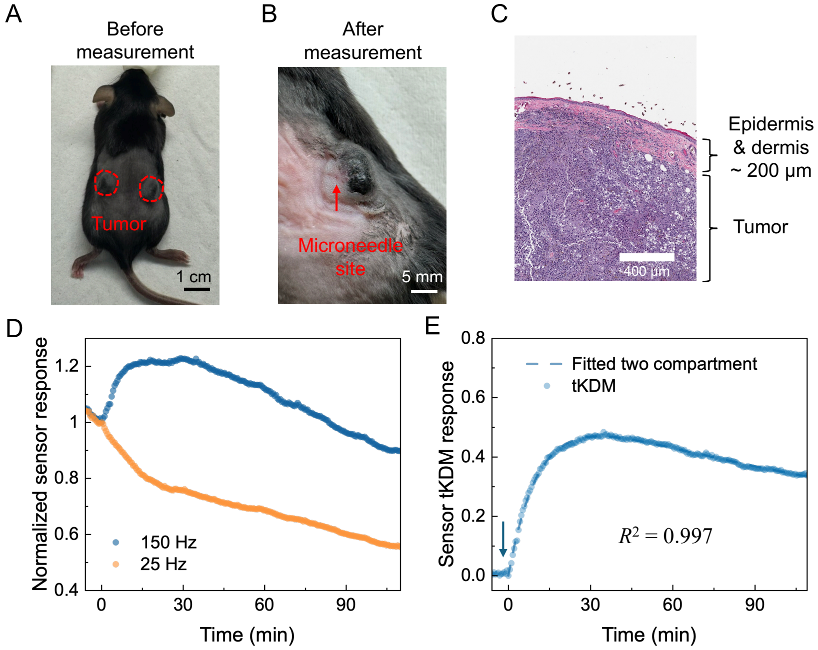

Fig. S27. Validation of tissue-specific kinetic differential measurement (tKDM) in a murine subcutaneous tumor. A. Photograph of an MC-38 tumor–bearing mouse prior to the experiment; tumor boundary outlined with a red dashed line. **B.** Post-experiment image showing the RNB sensor insertion site (arrow). **C.** H&E-stained section of the tumor, showing epidermis and dermis thickness of 200 μm (scale bar = 400 μm). **D.** Normalized SWV peak currents recorded at 150 Hz and 25 Hz following retro-orbital drug injection (40 mg/kg). **E.** tKDM response extracted from (D) and fit to Eq. 2 (dashed line, $R^2 = 0.997$). Arrow indicates time of drug administration. Mouse was under anesthesia throughout the recording.

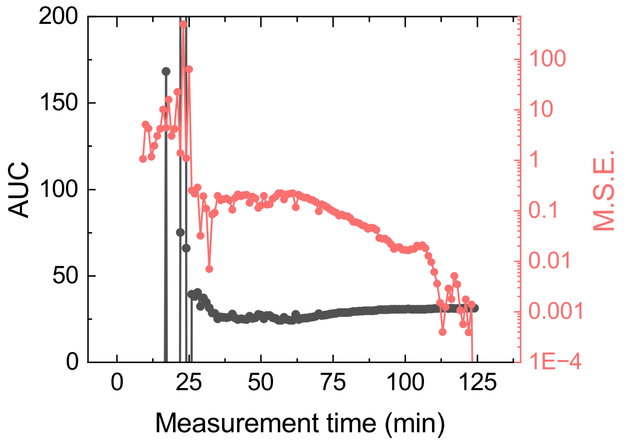

Fig. S28. AUC and fitting mean squared error (MSE) over measurement time in a measurement. The AUC represents area under the curve calculated from the Equation S11.

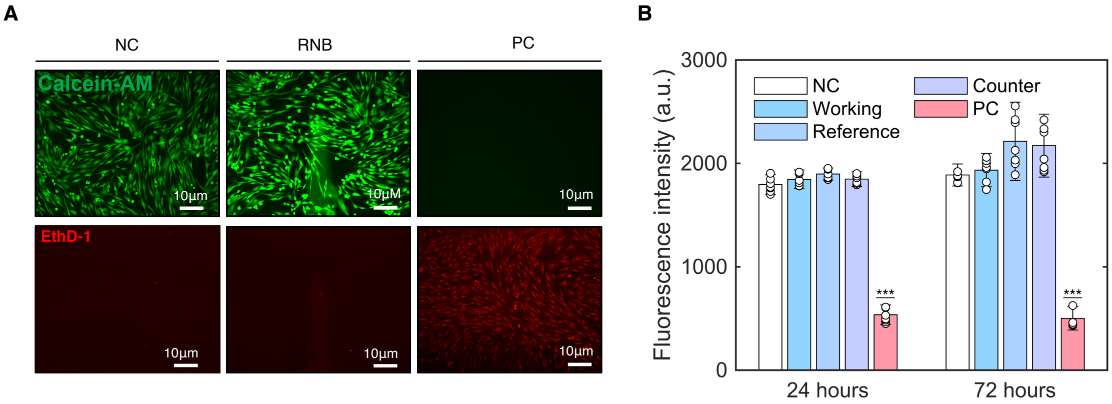

Fig. S29. RNB biocompatibility characterization. A, Morphology of HDFs cultured on the RNB stained for live (top image, green) and dead (bottom image, red) cells. **B**, Fluorescence intensity of live HDFs cultured with medium exposed to electrodes for 7 days. NC: negative control (growth media only); PC: positive control (growth media with 10 µg/mL $AgNO_3$). The error bars indicate the SD of two biological and two technical replicates. Bars without asterisks are not statistically significant ($P > 0.05$); (*** $P < 0.001$; two-tailed, two-sample *t*-tests).

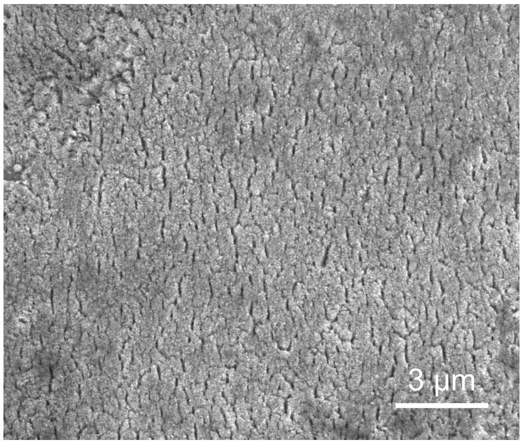

Fig. S30. Post-explantation surface morphology of RNB after six-day *in vivo* operation. Post-explantation SEM image shows no visible cracking or delamination, illustrating the mechanical stability of the nanostructured layer. Image acquired at an acceleration voltage of 10 kV.

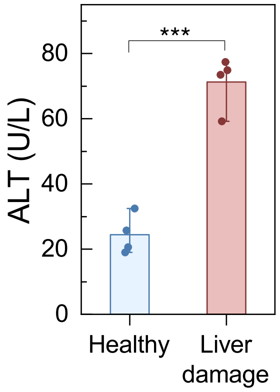

Fig. S31. Serum alanine transaminase (ALT) levels in rats without and with CCl_4 injection. $n = 4$, *** $P < 0.001$; two-tailed, two-sample t-test.

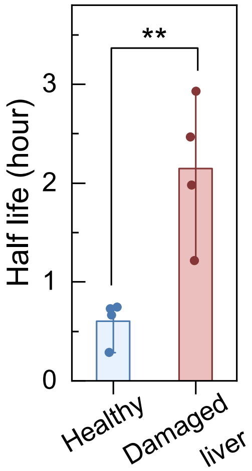

Fig. S32. Sensor-derived Half-life for healthy and acute liver-damaged rats. $n = 4$, ** $P < 0.01$; two-tailed, two-sample *t*-test.

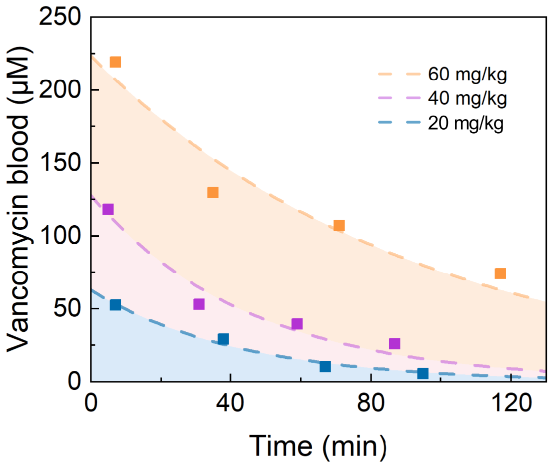

Fig. S33. Pharmacokinetic profiles of vancomycin in blood. Vancomycin concentrations measured by LC-MS over time in healthy rat administered with doses of 20 mg/kg, 40 mg/kg, and 60 mg/kg.

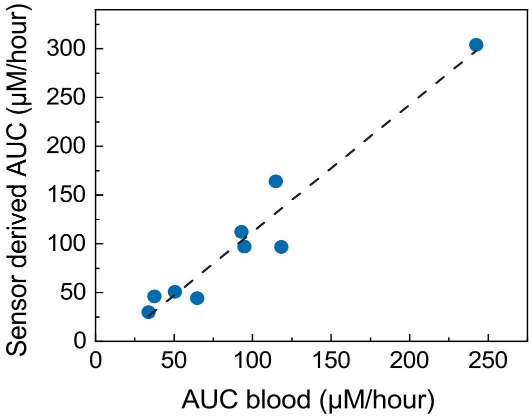

Fig. S34. AUC correlation. Correlation of the AUC between the RNB bioanalytical method using the device and blood quantification via LC-MS/MS for study 1.

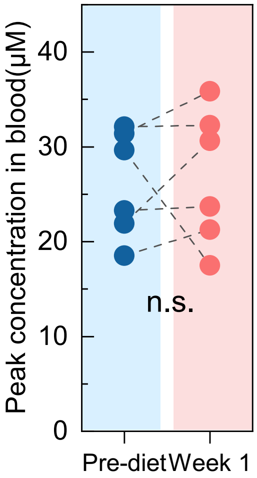

Fig. S35. Peak blood vancomycin concentration before and after one week of high adenine diet. “n.s.”: non-statistically significant; two-tailed, paired *t*-test, $n = 6$.

Table S1. Materials cost analysis of RNB aptamer sensor.

Component	**Cost (USD)**
Needles	0.15
PDMS	0.08
Homogenous gold layer	0.2
Co-sputtered Ag-Au layer (include machine hours)	0.25
Aptamer	0.67
Total	**1.35**

Table S2. In vivo microneedle and microprobe continuous electrochemical monolayer based biosensors.

	Signal enhancement	**Electrode footprint**	**Diffusion delay**	**Antifouling**	**Interfacial mechanical resilience**	**Self-deployability**	***In vivo* functionality**
RNB (this work)	Nanoporous	Small *(< 1 mm)*	In tissue	9 Days	Robust *(up to MPa)*	Wireless epidermal patch	6 days
CNC microneedle (*20*, *40*)	No	Large (array)	In tissue	N.D.	Exposed to tissue abrasion	Wireless epidermal patch	1 hour
Hydrogel microneedle(*43*)	No	Large *(array)*	~75 min $(d_{sampling} > 850\ \mu m)$	N.D.	N.A. *(No direct contact)*	Wired patch	2 hours
Magnetic implanted microneedle(*21*)	No	Large *(array)*	In tissue	N.D.	Exposed to tissue abrasion	Surgical implantation of magnet	2 hours
Dwell MN(*41*)	No	Large *(array)*	~50 min $(d_{sampling} > 690\ \mu m)$	N.D.	N.A. *(No direct contact)*	Wired patch	5 hours
Nanodendritic microneedle(*15*)	Nanodendrite	*Small* (< 1 mm)	In tissue	N.D.	Exposed to tissue abrasion	Wired patch	1 hour
Hollow microdevice(*39*)	Nanodendrite	Small *(< 1 mm)*	~ 26 min $(d_{sampling} > 500\ \mu m)$	No incubation time data	N.A. *(No direct contact)*	Wired patch	6 hours

N.D.: Not demonstrated; N.A.: Not applicable; Diffusion delay calculated based on vancomycin.

Data file S1. All individual-level tabular data.

Movie S1. Electrochemical failure mode of nanoporous needle electrode with conventional Ti adhesion. The nanoporous needle electrode, fabricated with a 50 nm Ti adhesion layer, exhibits a characteristic corrosion-induced failure mode. This video highlights the electrode's fragility, stemming from the limitations of conventional adhesion layers. Labels: WE/RE/CE - Working/Reference/Counter electrode.